Triple-clad W-type fiber mitigates multipath artifacts in multimodal optical coherence tomography

A. TANSKANEN,[1,2,*] J. MALONE,[1,2] G. HOHERT,[1] C. MACAULAY,[3] AND P. LANE[1,4,5]

[1] *Optical Cancer Imaging Lab, BC Cancer Research Institute, Vancouver, British Columbia V5Z 1L3, Canada*
[2] *School of Biomedical Engineering, University of British Columbia, Vancouver, British Columbia V6T 1Z4, Canada*
[3] *Department of Pathology and Laboratory Medicine, University of British Columbia and Vancouver General Hospital, Vancouver, BC, Canada*
[4] *School of Engineering Science, Simon Fraser University, Burnaby British Columbia V5A 1S6, Canada*
[5] *plane@bccrc.ca*
[*] *atanskanen@bccrc.ca*

Abstract: Multimodal endoscopic optical coherence tomography (OCT) can be implemented with double-clad fiber by using the presumed single-mode core for OCT and the higher numerical aperture cladding for a secondary modality. However, the quality of OCT in double-clad fiber (DCF) based systems is compromised by the introduction of multipath artifacts that are nt present in single-mode fiber OCT systems. Herein, the mechanisms for multipath artifacts in DCF are linked to its modal contents using a commercial software package and experimental measurement. A triple-clad W-type fiber is proposed as a method for achieving multimodal imaging with single-mode quality OCT in an endoscopic system. Simulations of the modal contents of a W-type fiber are compared to DCF and single-mode fiber. Finally, a W-Type fiber rotary catheter is used in a DCF-based endoscopic OCT and autofluorescence imaging (AFI) system to demonstrate multipath artifact free OCT and AFI of a human fingertip.

1. Introduction

Endoscopic optical coherence tomography (OCT) is potentially a useful imaging adjunct for a broad range of minimally invasive medical procedures. OCT systems require the use of single-mode fiber (SMF), as multimode fibers (MMF) or few-mode fibers (FMF) will cause the light backscattered into the fiber to couple into additional higher-order linearly-polarized (LP) modes, each with a unique group velocity [1].

In SMF OCT systems, the true image is carried in the fundamental LP_{01} mode. When MMF is used, light coupled into higher order modes (HOM) will result in separate ghost images. Given the interferometric nature of OCT, these HOM images become spatially displaced from the true image (corresponding to the fundamental LP_{01} mode) at delays proportional to the length of the fiber times the group delay difference of each HOM relative to the LP_{01} mode [2]. Although recent work takes advantage of HOMs differential response to scattering angles, these ghost images are typically undesirable as they can obscure the desired image if great care is not taken when setting the OCT systems reference arm [3,4]. The gold standard for fiber-based OCT is therefore SMF as the signal remains confined to only the LP_{01} mode, thus preventing multipath artifacts (ghost images). However, it is often desirable to add secondary imaging modalities to OCT without increasing the size of imaging catheters, which in turn requires the use of more complex optical fibers.

Often, a form of functional imaging (narrow-band reflectance, autofluorescence, fluorescence lifetime, multiphoton, second/third harmonic, etc) is paired with structural OCT. Other multi-modal approaches include coupling treatment methods, such as surgical lasers for ablation or photodynamic therapy, to OCT systems [5–8].

Our group has previously developed an OCT and autofluorescence imaging (OCT-AFI) system [9]. This system uses blue (450 nm) excitation, which allows for an assessment of collagen and elastin in the submucosa. The intensity of the endogenous fluorescence signal is modulated throughout cancer progression – though this may be confounded by other factors such as injury (wound healing) and inflammation [10,11]. Therefore, OCT is used to complement AFI by visualizing tissue morphology (epithelial tissue layers, microvasculature, subsurface ducts) to distinguish disease from confounders. An example of endoscopic multimodal imaging captured with this system is demonstrated in Fig. 1.
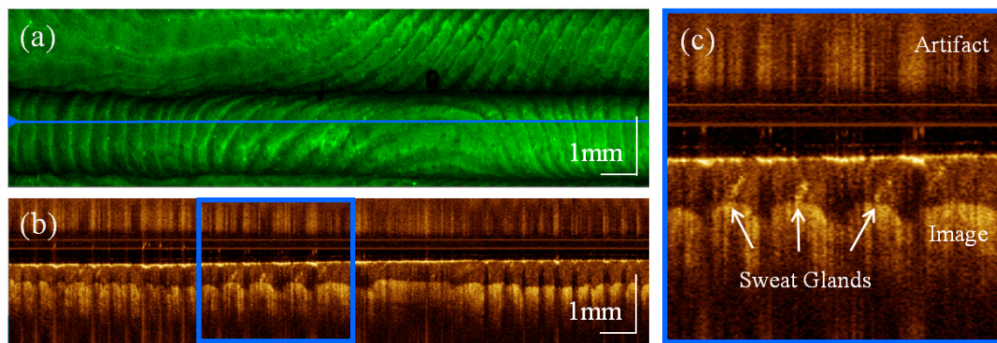

Fig. 1. Multimodal OCT-AFI of two human fingertips. a) *en-face* AFI view. b) longitudinal OCT B-Scan taken at the location of the blue line within the AF image in panel (a). c) Expanded view of the blue-bordered region portion of the longitudinal section in panel (b). Three bright sweat glands are visible within the epithelial layer as well as the fingerprint structure. Above the true image, an inverted and blurred ghost image artifact is visible.

To enable multimodal OCT in single-fiber endoscopes, double-clad fibers (DCF) are used. These fibers have a double-step refractive index profile (RIP) with a narrow single-mode core and a wide, high numerical aperture (NA) multimode cladding (Fig. 2(a)). To preserve single-mode transmission, the OCT signal is carried via the single-mode core whereas the multimode cladding provides a wider collection channel for low-light modalities which are insensitive to the dispersion of the numerous cladding modes. However, it is well established that using DCF compromises the image quality of OCT when compared to a SMF-based system [7,9,12]. This degradation appears as a diffuse and smeared artifact that obscures the desired image (Fig. 1(b) and 1(c)). This behaviour is understood to be a result of multipath artifacts which are generated when stray light is coupled into HOMs within the cladding before being cross-coupled back into the core at discontinuities in the fiber, such as splices.

Recently, we performed an investigation into the modal contents of DCF to further the understanding of how these inherent artifacts are generated [13]. Using the spatially and spectrally (S^2) resolved imaging method we established that a secondary core-like LP_{11} mode is prominently excited at wavelengths above the single-mode cut-off and that the group delay difference relative to the fundamental mode matched the delays between the OCT image and multipath artifact [14–16]. The DCF core's cut-off suggests this mode propagates through the cladding, but its transverse mode profile (TMP) is that of a core LP_{11} mode, which may cause additional coupling into the fundamental mode at discontinuities such as splices and prevent the effectiveness of components such as double-clad fiber couplers (DCFC) from being able to separate the signal from other cladding modes.
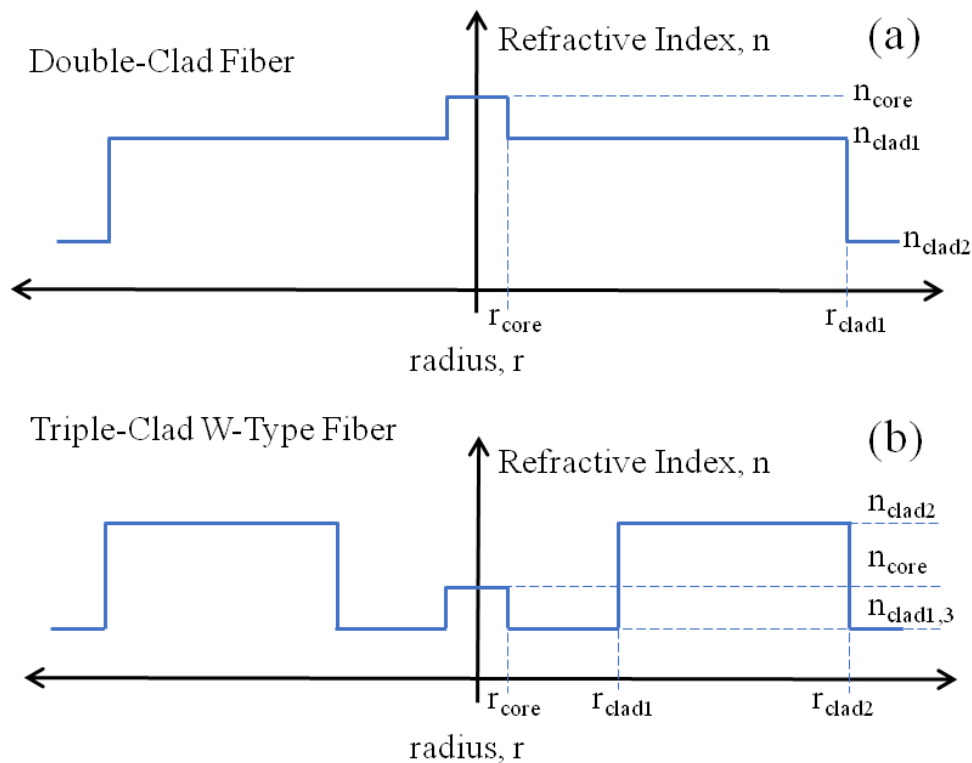
Fig. 2. Example refractive index profiles (n) as a function of fiber radius (r), for a) DCF and b) triple-clad W-Type fiber.

To our knowledge, there are no solutions which remove these multipath artifacts in DCF. Current approaches involve either adjusting the reference arm of the OCT system to mitigate the overlap between the image and the artifact or displacing the artifact outside of the systems imaging range using a sufficiently long length of DCF along the imaging arm. In practice, these approaches can be impractical to implement.

Many systems use fiber optic rotary joints (FORJs) which use a pair of lenses immersed in a coupling fluid to provide a means of catheter rotation. These are a prominent point of cross-coupling and the delays between the image and the multipath artifact can be mapped to the length of the catheter from the FORJ to the imaging tip. Using longer lengths of catheters would allow for the multipath artifact to be displaced, however FORJ-based imaging systems become increasingly susceptible to non-uniform rotational distortion as catheter length is increased [17].

Moreover, the axial point spread function (PSF) of the artifact is a smeared ghost of the true image PSF making it difficult to entirely prevent the artifact from superimposing the true image in complex samples. As such, it would be desirable to prevent the excitation of these artifacts entirely and allow for multimodal OCT systems to be designed around the confines of a clinical setting. Herein, we investigate the root cause of DCF multipath artifacts and build upon our previous work to propose a mechanism for their generation. Simultaneously, we contrast how a triple-clad W-Type fiber has more favorable modal properties that may allow for single-mode quality OCT in a single-fiber multimodal imaging system. The feasibility of this fiber for multimodal imaging is then tested using a pre-existing clinical OCT-AFI system.

2. W-Type fibers

W-Type refers to a type of optical fibers which have a core with a high index of refraction n, followed by a lower index first cladding and second cladding which has a higher index. Traditionally this profile leads to a decrease in the mode field diameter of the fundamental mode, which impacts bending loss when compared to a single-step fiber [18–20]. Of interest for this study is a triple-clad W-type fiber which has an additional cladding layer with the same index as the first depressed cladding and has a large diameter high index second cladding that acts as a multimode channel. An example RIP is shown in Fig. 2(b), where the core has a small diameter and a low index relative to the first cladding such that it is single-mode, and the second cladding is wide with a high index difference such that it is multimode.

The RIP of a W-Type fiber has several desirable properties: First, the first cladding layer has a lower index of refraction (n_{clad1}) than both the core (n_{core}) and the surrounding second cladding (n_{clad2}) to ensure that any components of core or second cladding modes become evanescent waves. Second, the outer (third) cladding layer is matched to the index of the first cladding which ensures that no modes can be supported within the first cladding. Lastly, the diameter of the first cladding layer must be sufficient to prevent a tunneling effect between the evanescent field components of the mode supporting layers [21,22]. We hypothesize that the core-cladding isolation of the W-Type fiber will allow for truly single-mode transmission through the fiber core and in turn prevent multipath artifacts in OCT. While the use of multi-clad fibers for dual-modality endoscopy has been described previously [23,24], to our knowledge, this is the first work describing the mechanisms through which triple-clad W-type fibers may mitigate multipath artifacts.

3. Simulating the modal content of multiclad fibers

Previously, we experimentally investigated the modal contents of both passive-doped DCF (SM-9/105/125-20A, Nufern, USA) and W-Type fiber (FUD-3318, Nufern, USA) using the S^2 imaging method [13]. A second HOM resembling the LP_{11} mode was found to propagate through the core of the DCF over wavelengths used within our OCT system (1310 ± 50 nm) and could be excited 100 nm above the rated cut-off for this fiber (1250 nm). The delay between this mode and the fundamental LP_{01} mode were found to correspond to delays between the image and the multipath artifacts OCT. Within the W-Type fiber a LP_{11} mode could be excited above the set cut-off of the fiber (1250 nm) but only propagated until 1290 nm. Here we add nuance to the mechanisms of multipath artifacts in OCT and explore the mechanisms by simulating the modal contents of each fiber.

The modes generated from models of the RIP of a SMF, the DCF, and the W-Type fiber are simulated using a commercial software package (RP Fiber Pro, RP Photonics). To compare the cores of each fiber, the same core profiles are used in each case: a theoretical 9 μm core diameter with a 1250 nm single-mode cut-off and a pure silica cladding. This profile mirrors the design of the cores for both the DCF and the W-Type fiber. Given the core radius, cladding index, and LP_{11} mode cut-off, the core index of each fiber can be calculated. For a single-step fiber, single-modality is achieved when the fiber's V-parameter satisfies,

$$V = r_{core}k_0\sqrt{n_{core}^2 - n_{clad}^2} < 2.405 \tag{1}$$

where r_{core} is the core radius, k_0 is the wavenumber, n_{core} is the core index, and n_{clad} is the index of the cladding. When the V-parameter is greater than 2.405 the LP_{11} fiber mode can propagate in addition to the fundamental mode. Based on this calculation, the following RIPs are simulated: a theoretical 9 μm core diameter SMF with a 1250 nm cut-off, a 9 μm core diameter DCF with a 1250 nm cut-off and a 105 μm pure silica multimode cladding; and a 9 μm core diameter W-Type fiber with a 1250 nm cut-off, a 40 μm pure silica first depressed index cladding, and a 105 μm

doped second multimode cladding. The geometries of each fiber are summarized in Table 1. In each RIP the first cladding follows the material dispersion curves for fused silica [25], and the core is assumed to vary according to [26,27],

$$n_{core}(\lambda) \;=\; \Delta n_{core}(\lambda_{cut}) \;+\; n_{clad1}(\lambda) \tag{2}$$

where $n_{core}(\lambda)$ is the spectral refractive index of the core, $\Delta n_{core}(\lambda_{cut}) = n_{core} - n_{clad1}$ is the refractive index difference between the core and the first cladding at the cut-off wavelength of the fiber λ_{cut}, and $n_{clad1}\lambda$ is spectral refractive index of the first cladding.

Table 1. Radii for each fiber type used for simulation

	SMF	DCF	W-Type	MMF
r_{core} (μm)	4.5	4.5	4.5	52.5
r_{clad1} (μm)	∞	52.5	20	∞
r_{clad2} (μm)	-	∞	52.5	-
r_{clad3} (μm)	-	-	∞	-

The refractive index of the second cladding is calculated given NA $\cong$ 0.2 at λ = 1550 nm and assuming the DCF cladding layers follow the standard relation for the NA of a step index fiber,

$$NA \;=\; \sqrt{n_{clad1}{}^2 - n_{clad2}{}^2} \tag{3}$$

where n_{clad2} is the index of the second cladding. Material dispersion for the second cladding layer is then calculated using the same assumption as for the core

$$n_{clad2}(\lambda) \;=\; \Delta n_{clad2}(1550\ nm) + \; n_{clad1}(\lambda) \tag{4}$$

where $\Delta n_{clad2}(1550\ nm) = \; n_{clad2} - n_{clad1}$ is the refractive index difference between the first and second cladding at 1550 nm.

The value for the W-Type fiber multimode cladding (NA $\cong$ 0.25) is provided on the datasheet at a wavelength of λ = 1550 nm. Material dispersion is added to the second cladding by applying Eq. (4) and given the first cladding layer is pure silica.

For each fiber, the propagation of the LP$_{11}$ mode is investigated at wavelengths close to cut off (1200 - 1350 nm). A mode is said to be a core mode when its effective refractive index n_{eff} satisfies,

$$n_{core} > n_{eff} > n_{clad1} \tag{5}$$

Conversely, within a multi-clad fiber, a mode is said to be a cladding mode when its effective refractive index satisfies,

$$n_{clad1} > n_{eff} > n_{clad2} \tag{6}$$

Within SMF, an alternative condition for cut-off is when the effective refractive index of that mode becomes equal to or less than the cladding index, and it will no longer be able to propagate.

Using the software package, we can both calculate the effective refractive index and visualize the changes in the TMP for the LP$_{11}$ mode within each fiber. The evolution of this mode will have implications in the formation of multipath artifacts. Figure 3(a) demonstrates the resulting effective refractive indices for the LP$_{11}$ mode within each fiber plotted adjacent to the index of the cladding (silica) as a function of wavelength around the presumed cut-off of 1250 nm. To better visualize the small changes around cut-off, the data is replotted as the change in effective refractive index relative to the silica cladding in Fig. 3(b).

From Fig. 3(a) and 3(b) we visualize that the LP$_{11}$ mode within the SMF achieves cut-off at the anticipated 1250 nm; however, for both the DCF and the W-Type fiber the additional cladding
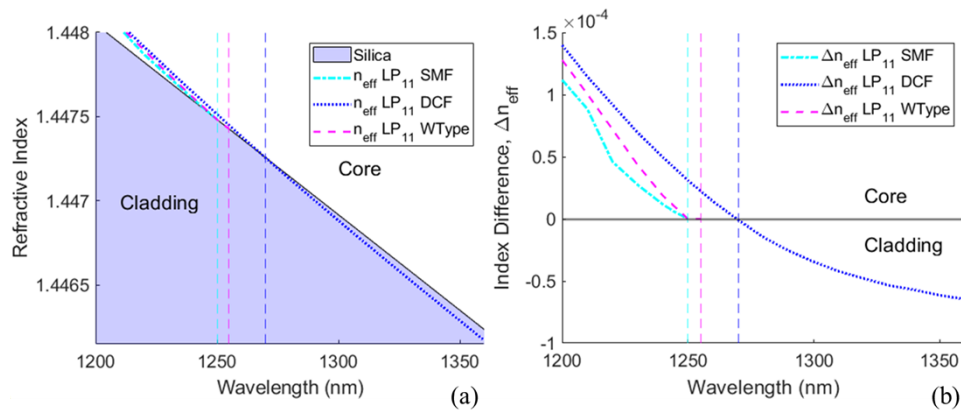
Fig. 3. Plots of the effective refractive indices of the LP_{11} mode within SMF (cyan), DCF (blue) and W-Type fiber (magenta), with equivalent core profiles and pure silica claddings, plotted as a function of wavelength. The cut-off for each fiber is denoted by a dashed vertical line. a) LP_{11} mode effective refractive index plotted adjacent to the index of silica. The shaded region indicates values of effective refractive index contained within the pure silica cladding. Above the shaded region corresponds to modes with effective refractive index within a doped core. b) LP_{11} mode effective refractive index difference relative to the index of pure silica. The SMF and the W-Type fibers are cut-off and cease to propagate when their indices become equal to that of silica ($\Delta n_{eff} = 0$) at 1250 and 1255 nm respectively. The effective refractive index of the DCF LP_{11} mode becomes equal to that of silica at 1270 nm but the mode continues to propagate at higher wavelengths as a cladding mode.

layers change the cut-off wavelength. For the W-Type fiber the effective refractive index of the LP_{11} mode becomes almost equal to that of silica at 1250 nm, and then it follows its index until 1255 nm before ceasing to propagate. For the DCF the cut-off is increased to 1270 nm, but the mode continues to propagate as a cladding mode over the examined wavelengs after the cut-off condition is achieved.

Examination of the TMP of the DCF LP_{11} mode before (1250 nm) and after (1270 nm) cut-off (Fig.4a and 4b) reveals its power remains confined to the area of the core in both cases. Even at the upper wavelengths emitted within our OCT system (1360 nm) the TMP of the LP_{11} mode is primarily within the core (Fig. 4(c)). It is not until approximately 1550 nm that the mode resembles what we would expect for a LP_{11} mode propagating through a multimode fiber (MMF) of the same size and index as the DCF first cladding (Fig. 4(d)).

The slow transition of the transverse mode profile from core modes to cladding modes as wavelength increases suggests that the DCF LP_{11}-like mode visualized within our previous work is the LP_{11} mode on the edge between fully core and fully cladding modes [13]. This would cause the DCF core to act as a two-mode fiber waveguide, rather than single-mode, leading to multipath artifact generation. However, the multipath artifact within DCF-based OCT is blurred in the A-line direction suggesting that there are additional modal interactions.

Thus, we examined higher order cladding modes within DCF and compared them to equivalent modes within a MMF, and W-Type fiber (Fig. 5). All simulations were conducted at 1310 nm. The MMF consists of only the multimode cladding portion of the DCF to illustrate the effect of the double-clad RIP on cladding modes. Equivalent modes were simulated within the triple-clad W-Type to illustrate the isolation effect of the depressed cladding layer. Selections of examined modes are shown in Fig. 5 (LP_{01}, LP_{11}, LP_{02}, and LP_{12}) to illustrate the unique properties of each fiber.
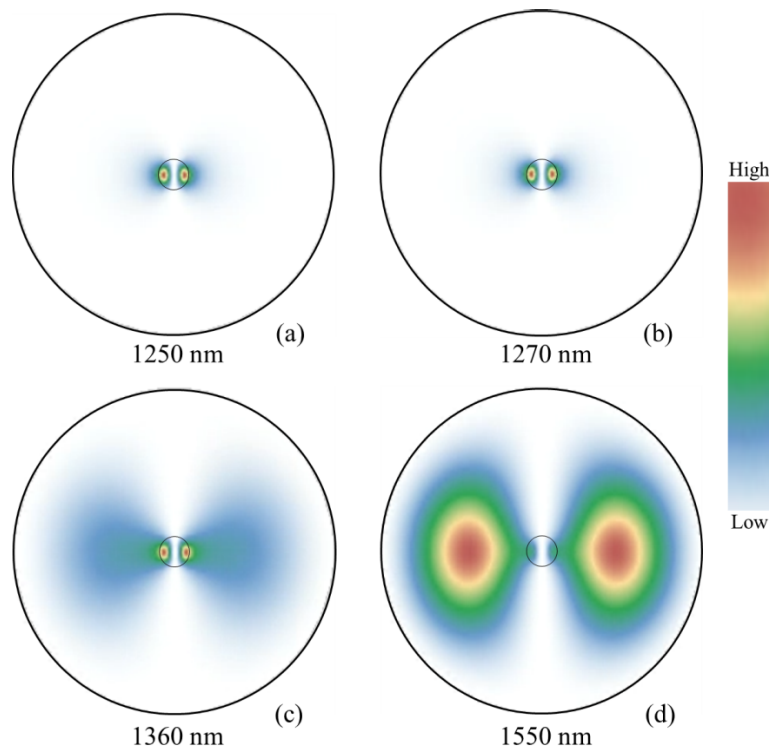
Fig. 4. Evolution of the LP_{11} modes transverse intensity profile within a DCF core at different wavelengths. a) LP_{11} core-mode before cut-off at 1250 nm. b) LP_{11} mode at cut-off, 1270 nm. c) LP_{11} cladding mode at 1360 nm, the highest wavelength reached by our swept source laser. d) LP_{11} cladding mode at 1550 nm fully expanded into the area of the cladding.

Examining the DCF simulation findings confirms that these modes are not confined to the core and cladding as defined by the effective refractive index. As expected, the fundamental LP_{01} mode has both the effective refractive index and transverse profile of a core mode. The effective refractive index of the LP_{11} mode suggests it is a cladding mode (above cut-off); however, its TMP is that of a LP_{11} core mode. The LP_{02} mode demonstrates similarly mixed core/cladding properties: while it has the effective refractive index of a cladding mode and most of the power is carried through the cladding, the central peak is compressed into the fiber core. Lastly, the LP_{12} cladding mode (and all other modes with the same azimuthal order) strongly resembles the LP_{11} mode, with the double lobed structure confined to the core but have smaller radial fringes within the cladding.

Contrasting these DCF simulations to a step index MMF shows an effect of compressing the TMP of most modes to the additional fiber layer (the core). Only within higher radial orders of the modes (LP_{02}, LP_{12}) do we see the power more confined to the center of the fiber, and in each case the central excitations remain far broader than in the DCF.

Simulations for the W-Type fiber demonstrate the impact of separating the single-mode core and multimode cladding with a depressed cladding layer. A separate LP_{01} mode is excited in both the core and the cladding. The cladding LP_{01} mode resembles a ring and remains isolated to the multimode second cladding. Each of the selected higher order cladding modes shows similar properties to their DCF counterparts, albeit with their power isolated solely to the multimode cladding. The LP_{01} core mode exists separate to these cladding excitations and resembles a
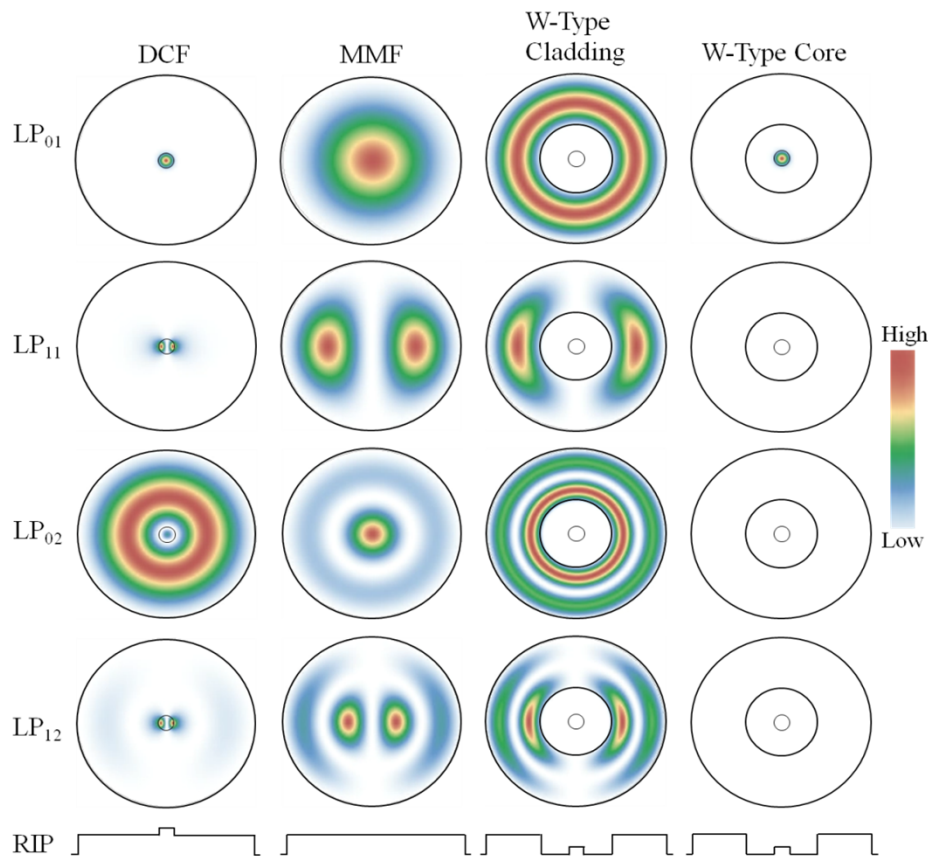
Fig. 5. Sample of modes within DCF, MMF, the third cladding of the W-Type fiber, and the core of the W-Type fiber at 1310 nm. Higher order cladding modes within the DCF are shown to be compressed into the area of the core when compared to a single-step multimode fiber with the same index as the DCF cladding. Within the W-Type fiber, only the LP_{01} mode is shown to propagate within the core, and the transverse intensity profile of the cladding modes does not overlap with the core. The bottom row illustrates the respective RIP cross sections for each fiber type.

standard SMF with the same core index profile. No higher order modes are excited within the core at this wavelength. We note that the software package considers all modes within the fiber and labels them in order of their effective refractive index. Given that the W-Type core has a lower refractive index than the second cladding (as in Fig. 2(b)), modes excited within the core are labelled as high order modes depending on the number of excited cladding modes with higher effective refractive index values. For ease of reference, we match the intensity profiles of core modes to the equivalent LP modes and relabel them accordingly.

The comparison between each of these fibers illustrates the potential advantages of using a triple-clad W-Type fiber in place of DCF for OCT applications: DCF suffers from a compression effect of the TMPs of higher order cladding modes into the core. It is likely that this increases the cross-coupling (crosstalk) between cladding modes and the fundamental core mode through fiber discontinuities along the imaging arm such as splices, connectors, or fiber optic rotary joints resulting from a potential increase in the overlap between the skewed exiting beam and the core of the accepting fiber. The increased coupling into these cladding modes could in turn result in the blurring of the multipath artifact along each OCT A-line. The core/cladding isolation in

W-Type fibers may be able to minimize this crosstalk across discontinuities in the case of small misalignments, as the first cladding layer would provide a buffer and attenuate the stray light.

4. Comparing core-cladding isolation between DCF and W-Type Fibers

To further investigate the properties of DCF and W-Type fiber visualized with simulation, an experiment was designed to measure the light transmitted through each fiber layer as a function of launch position. Light from a 1310 nm broadband source (BBS 1310 B-TS, AFC) was collimated and focused using a pair of aspheres (F280APC-C fiber collimator and A375TM-C, Thorlabs, Newton, New Jersey, USA) down to a ~4 μm diameter spot size on the cleaved face of a 60 cm long segment of test fiber (DCF or W-Type). The fiber and lens pair was mounted on a micrometer stage which allowed the focused spot to scan across the face of the fiber. The distal end of the fiber was mounted on a second micrometer stage and imaged through a long focal length objective lens (20X Plan Apo Infinity Corrected Long WD Objective, Mitotoyo, Japan) using a camera (STC – MBE132U3V, Sentech, USA) with a silicon detector. The micrometer stage with the lens pair couples the focused beam into the core of the fiber. This apparatus is illustrated in Fig. 6.
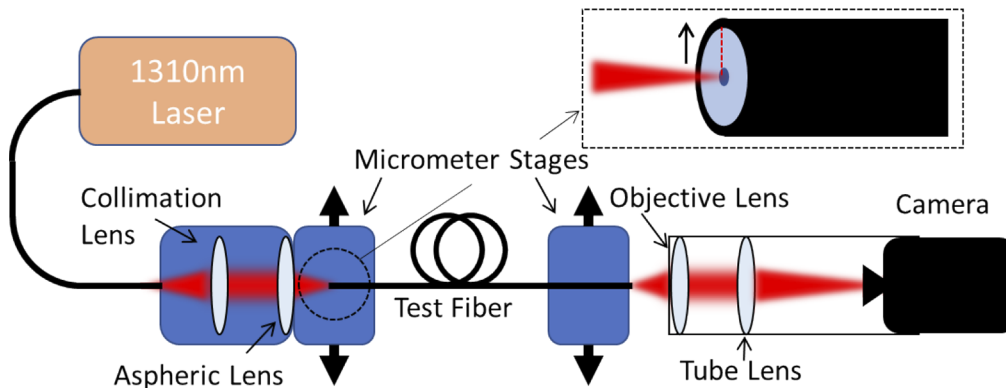

Fig. 6. Experimental setup used to image the light transmitted through a test fiber as a function of launch position along the cleaved back end of the fiber. Light from a 1310 nm broadband laser is focused into the test fiber at specific positions using a micrometer stage. A second stage is used to align the distal end of the fiber with an objective lens to image the fiber.

The beam is scanned in 1 μm steps across the back face of the test fiber, and the excited modes were imaged at each increment. The resulting images, along with a background image taken with the laser off, are used to calculate the total power coupled in the core and multimode cladding of both the DCF and the W-Type fibers. The total power within (1) the core and cladding of the DCF, and (2) the core and second cladding of the W-Type fiber are plotted as a function the position of the focused spot on the fiber, starting from the center of the fiber (Fig. 7). The reported power is normalized to the maximum total power travelling through all layers at highest transmission.

This experiment was also simulated using the commercial software package, using the same fiber profiles as described in Section 3. A Gaussian beam (1310 nm, 4 μm diameter) was coupled into each test fiber (DCF, W-Type) and was scanned across the back of the fiber in 1 μm steps. The total power coupled into the fundamental mode (LP_{01}) was assumed to be the power coupled into the core area, and the power in the remaining modes corresponds to the power within the cladding (second cladding for W-Type). We acknowledge that the experimentally measured power through each fiber layer is not equivalent to the proportion of power coupled into the
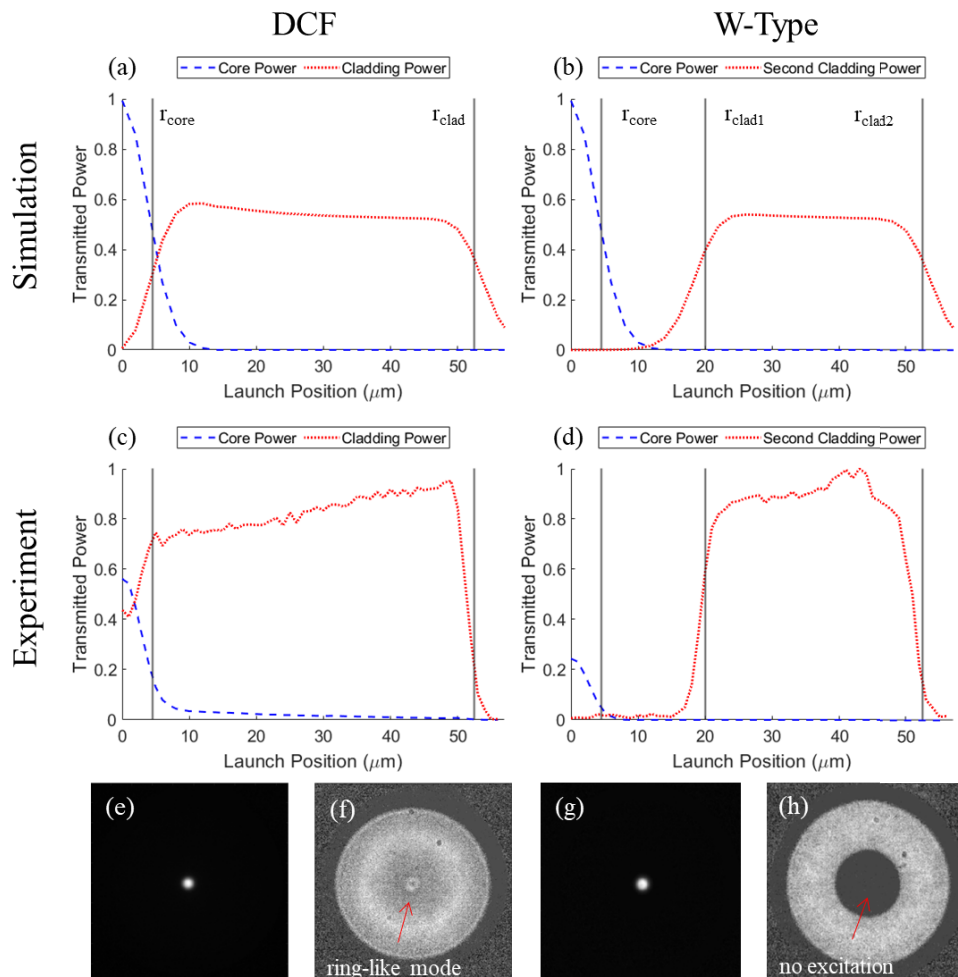
Fig. 7. a) Simulated power coupled into the core and cladding modes of a DCF as a function of the position of a 4 μm Gaussian beam used to excite the modes. b) Simulated power coupled into the core and cladding modes of W-Type fiber as a function of the position of a 4 μm Gaussian beam used to excite the modes. c) Transmitted power through the core and the cladding of a DCF measured experimentally as a function of the position of a 4 μm focused beam along its cleaved input. The transmitted power in each layer is normalized to the maximum total power achieved through both layers. The two vertical lines at 4.5 μm and 52.5 μm correspond to the geometric radii of the core and the cladding respectively. d) Transmitted power through the core and the second cladding of the W-Type fiber measured experimentally as a function of the position of a focused beam along its cleaved input. The three vertical lines at 4.5 μm, 20 μm and 52.5 μm correspond to radii of the core, first cladding and second cladding respectively. e) Image of the illuminated core of a DCF. f) Image of the illuminated cladding of the DCF. g) Image of the illuminated core of the W-Type fiber. h) Image of the illuminated second cladding of the W-Type fiber showing no excitation in the core.

core mode versus the cladding modes. This methodology is chosen due to the constraints of the simulation software.

The simulated and experimentally measured core and cladding powers were plotted starting from the center of the fiber, as a function of the launch position used to excite the modes within the fiber for both the DCF and W-Type in Fig. 7. The simulated power transmitted through the DCF and W-Type are displayed in Fig. 7(a) and 7(b) and the experimentally measured powers are shown in Fig. 7(c) and 7(d).

The simulation and experimental results presented in Fig. 7 show that significantly more power is cross-coupled between the core and cladding of the DCF fiber as compared to the W-Type fiber. Experimentally, when focused directly into the core of the DCF (Fig. 7(c)), only ~60% of the total power is confined to the core, with the remaining ~40% coupled into the cladding. Within 5 μm the cumulative power within the cladding is equal to that of the core, even while the beam is primarily focused into the core. As the beam is moved across the fiber and into the cladding, most of the signal becomes coupled into the cladding. However, we see in Fig. 7(c) that a small amount of power (<10%) remains coupled into the core of the DCF even when the beam is entirely focused into the cladding. Qualitatively, we can visualize this in Fig. 7(f) as a ring-like excitation within the core of the fiber when the cladding is illuminated. We speculate this excitation is the summation the TMPs of cladding modes which carry power through the core (as explored in section 3). A lesser degree of core-to-cladding cross-coupling is expressed in the DCF simulation when compared to experiment (Fig. 7(a)), where the percentage of power coupled into the fundamental core mode drops to 0 after a 12 μm displacement from the center in the excitation beam. This discrepancy is likely caused due to differences in classification of modes between the experimental and simulated models: the power from core-like cladding modes ($n_{eff} < n_{clad}$) is accounted for as cladding modes within simulation, whereas much of the power coupled into these modes would be accounted for as core power within experiment.

At first glance when comparing the percentage of power coupled into the cores of each fiber, more power appears to be coupled into the DCF core (Fig. 7(c)) than the W-Type core (Fig. 7(d)) at the 0 μm launch position. However, as the plots in Fig. 7 are normalized to the total transmitted power, this may be due to an increase in transmission in the cladding rather than a decrease in the core. One limitation of this experiment is the same lens pair was used for both fibers. These lenses focus light to angles *greater* than the NA of the DCF cladding but *less* than the NA of the W-Type cladding (NA $\cong$ 0.22 for the lens pair, NA $\cong$ 0.2 for the DCF cladding, NA $\cong$ 0.25 for the W-Type cladding). Some of the higher-angle illumination that is lost in the DCF cladding may be captured in the W-Type cladding, resulting in a lower normalized power in the core of the W-Type. Additionally, we expect some cladding modes to be excited at a 0 μm launch position as some power is measured to be transmitted through the cladding at this point. The components of the cladding modes which propagate through the geometric area of the core would contribute to an increase in power through this area.

As anticipated, the first cladding layer of the W-Type fiber causes a definitive separation between core and second-cladding modes. This is readily visualized in Fig. 7 (g) and 7 (h), which show qualitatively that cladding and core can be excited in isolation from each other. Experimentally, we find that the core of the W-Type fiber is only excited when the excitation beam is coupled into the core, and modes within the second cladding are only excited when the excitation beam overlaps with this layer (Fig. 7(d)). There is almost no transmission when the beam is focused into the depressed first cladding. These measurements are reflected in the simulation (Fig. 7(b)) where the cladding is not excited when light is directed into the core and the core remains dark with cladding illumination. Considering these experiments, and the simulations presented in Section 4, the depressed cladding layer of the W-Type fiber may be sufficient to allow for the core to transmit light in a manner comparable to a single-mode fiber.

5. Single-mode quality OCT with a W-type fiber catheter

To confirm the utility of W-Type fiber for multimodal imaging, and to further explore whether this fiber would reduce multipath artifacts in OCT, we collected images using a W-Type fiber catheter on a pre-existing endoscopic OCT-AFI system [9]. Previously, we determined that the multipath artifacts which degrade the quality of OCT imaging are excited at the end of the catheter and are cross-coupled at the FORJ [13]. This suggests we only need to employ W-Type fiber in the catheter to mitigate the multipath artifacts.

A W-Type catheter is fabricated in the same fashion as previously reported [9], and used in place of a DCF catheter with the OCT-AFI system shown in Fig. 8. The OCT sub-system has a 1310 ± 50 nm emission band, 25 mW output power swept source laser SSOCT-1310, Axsun Technologies Inc., Billerica, MA, USA) and a SMF Mach-Zehnder interferometer (MZI) with a balanced photodetector (PDB420C, Thorlabs, Newton, New Jersey, USA). AFI excitation light is generated by a 450 nm (LP450-SF15, Thorlabs, Newton, New Jersey, USA) blue laser. The infrared and blue light emitted through the sample arm is combined via a wavelength division multiplexer (WDM). A DCF FORJ (Princetel) and custom rotary pullback drive allows for rotation and retraction of the imaging catheter in a helical scan pattern for volumetric imaging of luminal organs. Light is emitted and collected from the in-house fabricated imaging catheter. Along the return path, infrared OCT signal coupled through the core is separated from the green autofluorescence excitations in the cladding using a DCFC (DC1300LEFA, Thorlabs, Newton, New Jersey, USA) with the core signal returning to the MZI and the light coupled into the
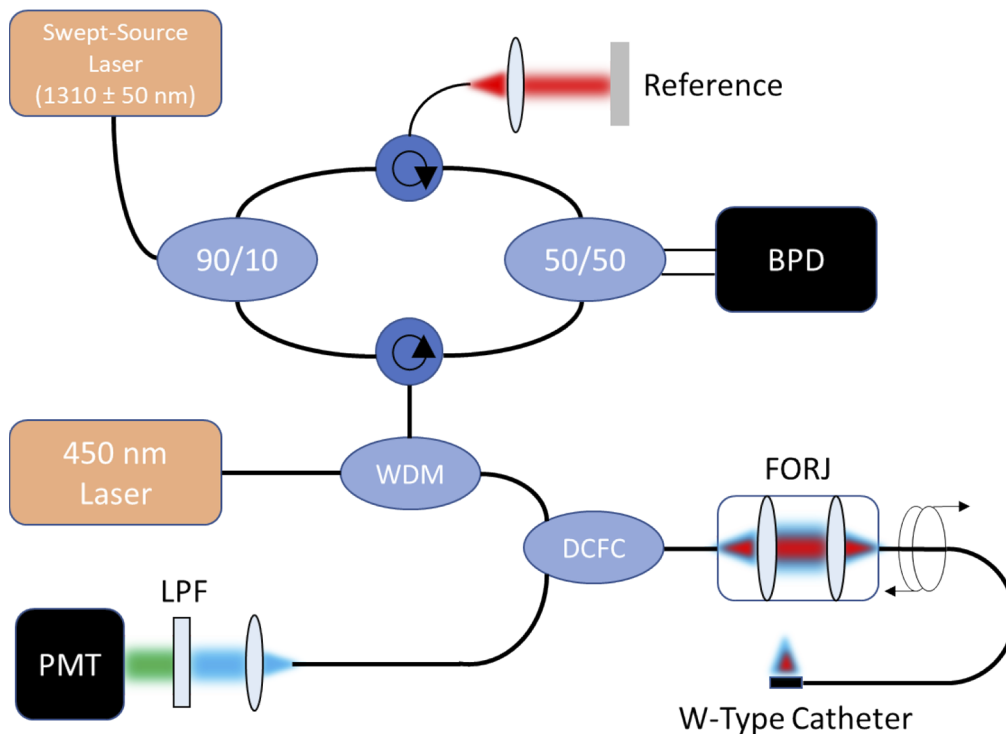

Fig. 8. Schematic of the endoscopic OCT-AFI system used to verify the capabilities of a triple-clad W-Type fiber for multimodal imaging. A W-Type rotary probe is used in place of a standard DCF catheter. BPD: balanced photodetector, WDM: wavelength division multiplexer, LPF: long-pass wavelength filter, PMT: photomultiplier tube, DCFC: double-clad fiber coupler, FORJ: fiber optic rotary joint.
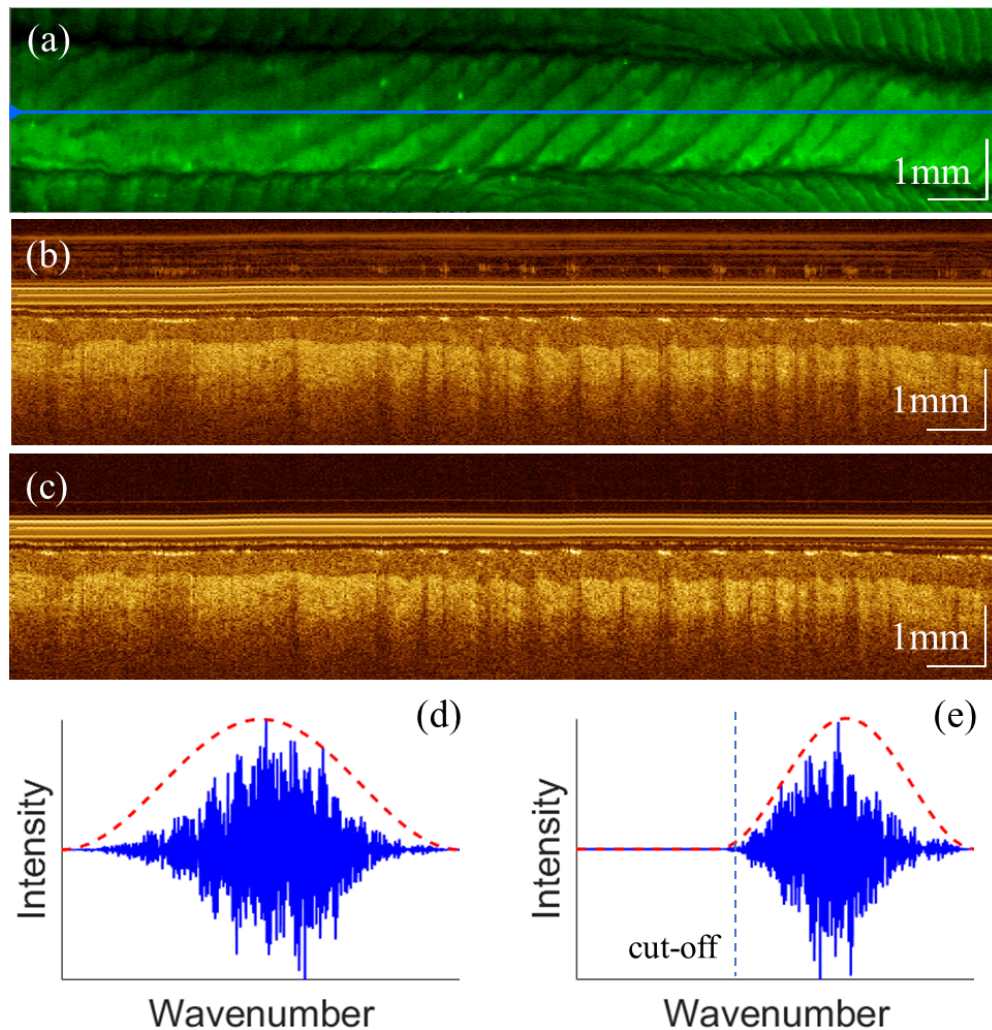
Fig. 9. Multimodal OCT-AFI of a human fingertip taken using a W-Type fiber-based catheter. a) Autofluorescence image. b) OCT B-Scan taken at the location of the blue line in (a). This B-Scan shows a multipath artifact resulting from the LP_{11} mode as excess bands of noise at the top of the panel. c) The same B-Scan as in (b) after the apodization filter has been reduced to only allow wavelengths after the cut-off of the LP_{11} mode. d) Reference A-Line in k-space after apodization with a Hamming filter which allows the entire spectrum. This A-line corresponds to those forming the image in (b) before Fourier processing. e) Reference A-Line in k-space after apodization with a Hamming filter which allows only higher wavelengths. This A-line corresponds to those forming the image in (c) before Fourier processing.

cladding being passed into a PMT (H9433-201, Hamamatsu, Japan) with a 480 nm long pass wavelength filter (E480LPXT, Chroma, Bellows Falls, VT, USA) for autofluorescence detection.

Multimodal imaging is performed on a human fingertip (Fig. 9). AFI of the fingertip imaged with the W-Type catheter (Fig. 9(a)) is resolved at a comparable quality to AFI taken with a standard DCF catheter (Fig. 1(a)). An examination of an OCT B-Scan shows that while W-Type fiber is capable of performing adequate OCT, a multipath artifact is still excited (Fig. 9(b)).

If the multipath artifact corresponds to a LP_{11} mode, this finding is both expected and easily mitigated. The LP_{11} mode cut-off in this W-Type fiber is 1290 nm as measured experimentally in a previous study, which is within the imaging band of this OCT-AFI system. By adjusting the apodization window used prior to Fourier processing, OCT can be constructed only using wavelengths above cut-off and thus the LP_{11} mode can be removed. Instead of processing the whole spectrum of our swept source laser contained within each A-Line (Fig. 9(d)) in k-space of the tomogram is filtered using a shortened Hamming window (Fig. 9(e)) to only allow for values corresponding to wavelengths above the single-mode cut-off. After filtering, the multipath artifact is removed (Fig. 9(c)), supporting our hypothesis. Additionally, we demonstrate that no multipath artifacts are generated by the remaining DCF within the system. While it is likely that light is cross-coupled into the HOMs of the DCF within the FORJ, this signal passes through a DCFC which separates the cladding light into a separate channel. On the return path just past the DCFC there is a standard fiber joint connecting DCF to SMF. Past this point, residual cladding signal will be attenuated within the cladding of the SMF. Any signal which is then cross-coupled between the HOMs of the DCF and the SMF fundamental mode is not detected within our system

We compare OCT images of a human fingertip generated using a SMF (Fig. 10(a)), DCF (Fig. 10(b)) and W-Type catheter (Fig. 10(c)). Each image is processed using the shortened apodization window to match axial resolutions. Using a subset of the spectrum does not appear to have had a deleterious impact on the OCT quality or ability to resolve biologically relevant features (fingerprints, sweat glands, epithelium, stroma). We calculate that digitally reducing the bandwidth to wavelengths above the LP_{11} cut-off (1290–1360 nm) will reduce the axial resolution from 7.6 μm to 11.7 μm in air. In the images, we observe that the multipath artifact present in DCF (Fig. 10(b)) remains prominent at this region of the spectra as cut-off is not achieved. The SMF (Fig. 10(a)) and W-Type (Fig. 10(c)) images do not have an artifact and demonstrate an increase in image quality. The image quality in the W-Type (Fig. 10(c)) image is comparable to the SMF (Fig. 10(a)) image, and thus we conclude that W-Type probes are capable of single-mode quality OCT.
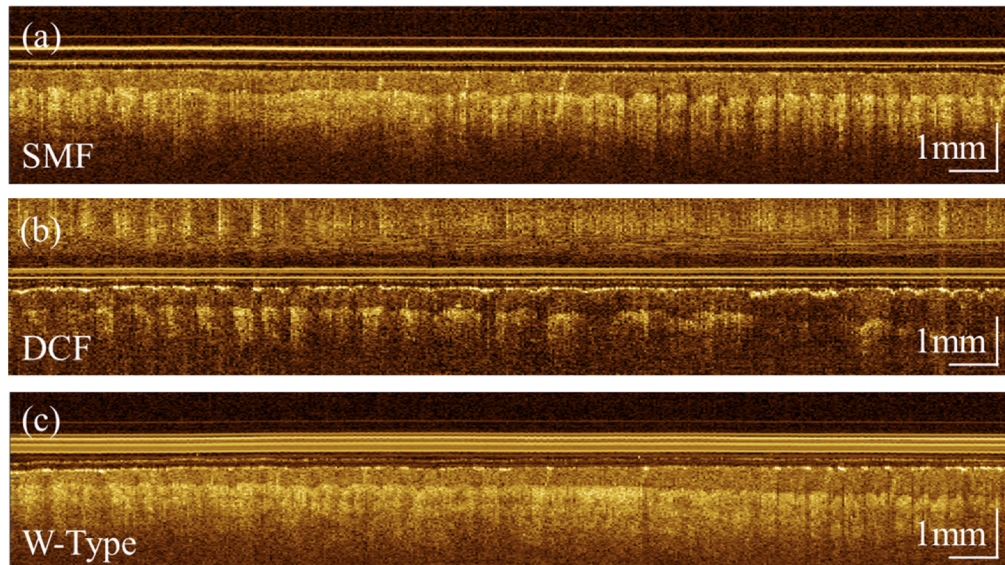

Fig. 10. Comparison of OCT images of a human fingertip taken using catheters with different optical fibers a), a SMF catheter b), a DCF catheter and c) a W-Type fiber catheter. A reduced Hamming window corresponding to the wavelengths above the LP_{11} cut-off of the W-Type fiber is applied to the k-space A-Lines in each image to match axial resolutions.

6.   Discussion

This work demonstrates the advantages of using triple-clad W-Type fiber in place of DCF in multimodal endoscopic imaging applications. The addition of a depressed cladding layer which separates the single-mode core from the multimode cladding of the fiber addresses multipath artifacts in DCF-based OCT by (1) limiting the cross-coupled power of cladding modes to the core and (2) ensuring the cut-off modes do not continue to propagate through the multimode cladding. These effects enable development of endoscopic probes which provide single-mode quality OCT alongside a secondary imaging domain.

Beyond the capabilities of W-Type fiber for multimodal imaging, this paper is a study on how the modal properties of DCF are detrimental to OCT imaging. While not commonly stated in literature on the design of multimodal imaging systems, the implicit assumption is that the core and the cladding of DCF are separate channels, where a presumed single-mode core collects scattered light for OCT imaging, and a multimode cladding collects signal for the secondary domain. Both simulations and experiment demonstrate that, in practice, these two light transmitting layers of the fiber cannot be treated as independent channels. For example, in Fig. 3(b), the cut-off wavelengths of HOMs within the core of the fiber are higher in multi-clad fibers than expected for a SMF. Moreover, these are not truly *cut-off* in double-clad fibers: rather, when the effective refractive index of a mode becomes equal to that of the cladding (cut-off in a SMF) the mode continues to propagate as a *cladding mode*. Despite this name, the TMP remains confined to the area of the core well after cut-off as explored in Fig. 4.

Moreover, if we analyze HOMs within the cladding, the addition of a single-mode core to a high NA multimode fiber compresses the TMP of HOMs when compared to a MMF of the same diameter. Specifically, the central excitations of LP modes with low azimuthal orders are drawn towards the fiber core when compared to a single-step multimode fiber (Fig. 5). This effect is likely the cause for the large percentage of transmission in the cladding of DCF when light is focused into the fiber core (Fig. 7(a) and 7(c)). Focusing a Gaussian beam into the fiber core will prominently excite not only the fundamental mode travelling through the core, but also cladding modes (including those with core excitation). Equivalently, when light is coupled directly into the cladding these central excitations carry a substantial percentage of the total power through the core. Thus, DCF containing (1) core-like cladding modes close to cut-off and (2) compressed central excitations in cladding modes causes core behavior more akin to a few-mode fiber than a truly single-mode waveguide.

In our previous work, an LP_{11}–like mode was detected within the core of DCF that corresponded to the edge position of multipath artifacts. However, this model (analogous to a two-mode fiber) would cause a sharper excitation than what is observed. Even considering intra-modal dispersion, the observed blurring effect extends from the edge of the multipath artifact to the image. We postulate that the smearing of the axial PSF is caused by the HOMs in the cladding excited by light coupled into the core. These modes could provide additional channels for cross-coupling when mechanical stress is induced via phenomena such as flexing and vibrations from the helical scanning pattern of a FORJ [28]. Fully realizing this mechanism would require investigation into the specific cladding modes (in addition to the LP_{11} mode) which contribute to multipath artifacts and how the dispersion and group velocities of these modes (relative to LP_{01}) cause the axial blurring.

A downside of using triple-clad W-Type fiber instead of DCF is the potential reduction in surface area of the cladding annulus compared to that of DCF owing to the first depressed cladding layer. The smaller cladding annulus would naturally reduce the collection efficiency through this optical channel and could compromise the signal-to-noise ratio (SNR) of low-signal modalities, such as AFI. However, in the OCT-AFI tests, the W-Type catheter collected AFI with a comparable SNR to a standard DCF. The use of AFI is notable here as a low-signal modality: while the excitation of endogenous fluorophores is of interest in many disease applications and

reduces the need for contrast agents and dyes, it suffers from poor SNR when compared to exogenous fluorescence. The finding that AFI quality did not suffer in this W-Type catheter is promising for potential clinical applications.

One limitation owing to the particular W-Type fiber used in this work is that the LP_{11} mode did not achieve cut-off before the lower wavelength of the swept source laser used for imaging. This required digitally filtering to remove wavelengths below cut-off. Naturally, filtering away part of the imaging band will result in a decrease in axial resolution (from 7.6 to 11.7 μm); although this effect is difficult to parse from the increase in image quality by removal of the multipath artifact when comparing Fig. 9(b) and 9(c). A W-Type fiber RIP with a lower core index could be fabricated to decrease the cut-off wavelength as per Eq. (1). For example, the RIP used for the simulations presented in this work resulted in a cut-off wavelength of 1255 nm, which is outside of the spectral range of the laser used in this OCT system.

7. Conclusion

The experiments and simulations performed herein demonstrate the need for an alternative to DCF for multimodal endoscopic imaging. A double-step refractive index profile is shown to change the transverse mode profile of cladding modes such that their central excitations can more readily interfere with the fundamental core mode. This effect is deleterious to the quality of OCT images as the cores of DCFs will therefore operate more akin to a few-mode fiber causing the generation of multipath artifacts. As an alternative, a triple-clad W-Type fiber with a depressed cladding layer separating the core and multimode cladding provides isolation between light transmitting layers to allow for single-mode quality OCT. The capabilities of W-Type fibers were tested in place of a DCF-based catheter using a previously constructed OCT-AFI system and demonstrated single-mode quality OCT. Further work is needed to determine W-type fibers' capabilities with other functional imaging modalities.

References

1. T. Xie, D. Mukai, S. Guo, M. Brenner, and Z. Chen, "Fiber-optic-bundle-based optical coherence tomography," Opt. Lett. **30**(14), 1803 (2005).
2. J. H. Han and J. U. Kang, "Effect of multimodal coupling in imaging micro-endoscopic fiber bundle on optical coherence tomography," (2012), doi: 10.1007/s00340-011-4847-y.
3. M. P. de Sivry-Houle, S. B. Beaudoin, S. Brais-Brunet, M. Dehaes, N. Godbout, and C. Boudoux, "All-fiber few-mode optical coherence tomography using a modally-specific photonic lantern," Biomed. Opt. Express **12**(9), 5704 (2021).
4. P. Eugui, A. Lichtenegger, M. Augustin, D. J. Harper, M. Muck, T. Roetzer, A. Wartak, T. Konegger, G. Widhalm, C. K. Hitzenberger, A. Woehrer, and B. Baumann, "Beyond backscattering: Optical neuroimaging by BRAD," arXiv, arXiv:1712.00361 (2017).
5. K. Beaudette, W. Lo, M. Villiger, M. Shishkov, N. Godbout, B. E. Bouma, and C. Boudoux, "Towards in vivo laser coagulation and concurrent optical coherence tomography through double-clad fiber devices," (2016), doi: 10.1117/12.2209382.
6. S. A. Boppart, J. Herrmann, C. Pitris, D. L. Stamper, M. E. Brezinski, and J. G. Fujimoto, "High-resolution optical coherence tomography-guided laser ablation of surgical tissue," J. Surg. Res. **82**(2), 275–284 (1999).
7. K. Beaudette, H. W. Baac, W. J. Madore, M. Villiger, N. Godbout, B. E. Bouma, and C. Boudoux, "Laser tissue coagulation and concurrent optical coherence tomography through a double-clad fiber coupler," Biomed. Opt. Express **6**(4), 1293 (2015).
8. K. Beaudette, M. Strupler, J. Ren, B. E. Bouma, and C. Boudoux, "Radiometric model for coaxial single- and multimode optical emission from double-clad fiber," Appl. Opt. **57**(5), 1110 (2018).

9. H. Pahlevaniezhad, A. M. Lee, T. Shaipanich, R. Raizada, L. Cahill, G. Hohert, V. X. Yang, S. Lam, C. MacAulay, and P. Lane, "A high-efficiency fiber-based imaging system for co-registered autofluorescence and optical coherence tomography," Biomed. Opt. Express **5**(9), 2978 (2014).

10. M. Cicciù, G. Cervino, L. Fiorillo, C. D'Amico, G. Oteri, G. Troiano, K. Zhurakivska, L. Lo Muzio, A. S. Herford, S. Crimi, A. Bianchi, D. Di Stasio, R. Rullo, G. Laino, and L. Laino, "Early diagnosis on oral and potentially oral malignant lesions: A systematic review on the Velscope® fluorescence method," Dentistry Journal **7**(3), 93 (2019).

11. I. Pavlova, M. Williams, A. El-Naggar, R. Richards-Kortum, and A. Gillenwater, "Understanding the biological basis of autofluorescence imaging for oral cancer detection: High-resolution fluorescence microscopy in viable tissue," Clin. Cancer Res. **14**(8), 2396–2404 (2008).

12. F. Feroldi, M. Verlaan, H. Knaus, V. Davidoiu, D. J. Vugts, G. A. M. S. van Dongen, C. F. M. Molthoff, and J.F. de Boer, "High resolution combined molecular and structural optical imaging of colorectal cancer in a xenograft mouse model," Biomed. Opt. Express **9**(12), 6186 (2018).

13. A. Tanskanen, G. Hohert, A. Lee, and P. Lane, "Higher-Order Core-Like Modes in Double-Clad Fiber Contribute to Multipath Artifacts in Optical Coherence Tomography," J. Light. Technol. **39**(17), 5573–5581 (2021), doi: 10.1109/jlt.2021.3088055.

14. J. W. Nicholson, A. D. Yablon, S. Ramachandran, and S. Ghalmi, "Spatially and spectrally resolved imaging of modal content in large-mode-area fibers," Opt. Express **16**(10), 7233 (2008).

15. D. M. Nguyen, S. Blin, T. N. Nguyen, S. D. Le, L. Provino, M. Thual, and T. Chartier, "Modal decomposition technique for multimode fibers," Appl. Opt. **51**(4), 450 (2012).

16. J. Jasapara and A. D. Yablon, "Spectrogram approach to Sˆ2 fiber mode analysis to distinguish between dispersion and distributed scattering," Opt. Lett. **37**(18), 3906 (2012).

17. G. van Soest, J. G. Bosch, and A. F. W. van der Steen, "Azimuthal registration of image sequences affected by nonuniform rotation distortion," IEEE Trans. Inf. Technol. Biomed. **12**(3), 348–355 (2008).

18. S. Kawakami and S. Nishida, "Perturbation Theory of a Doubly Clad Optical Fiber with a Low-Index Inner Cladding," IEEE J. Quantum Electron. **11**(4), 130–138 (1975).

19. T. P. Tanaka, S. Yamada, M. Sumi, and K. Mikoshiba, "Microbending losses of doubly clad (W-type) optical fibers," Appl. Opt. **16**(9), 2391 (1977).

20. H. J. Hagemann, H. Lade, J. Warnier, and D. U. Wiechert, "The Performance of Depressed-Cladding Single-Mode Fibers with Different b/a Ratios," J. Light. Technol. **9**(6), 689–694 (1991).

21. T. Hayashi, T. Taru, O. Shimakawa, T. Sasaki, and E. Sasaoka, "Design and fabrication of ultra-low crosstalk and low-loss multi-core fiber," Opt. Express **19**(17), 16576 (2011).

22. G. Rademacher, R. S. Luís, B. J. Puttnam, Y. Awaji, and N. Wada, "Crosstalk dynamics in multi-core fibers," Opt. Express **25**(10), 12020 (2017).

23. 魏晋, "A kind of optical fiber and imaging method of integrated optical coherence and incoherent imaging system," CN107518862A, Dec. 29, 2017.

24. G. J. Tearney, B. E. Bouma, H. Yoo, M. Shishkov, J. Gardecki, R. Shubochkin, T. Morse, and A. F. Jaffer, "Systems, devices, methods, apparatus and computer-accessible media for providing optical imaging of structures and compositions," US9557154B2, Jan. 31, 2017.

25. I. H. Malitson, "Interspecimen Comparison of the Refractive Index of Fused Silica*,†," J. Opt. Soc. Am. **55**(10), 1205 (1965).

26. G. Świrniak and J. Mroczka, "Numerical analysis of primary rainbows from a homogeneous cylinder and an optical fiber for incident low-coherent light," J. Quant. Spectrosc. Radiat. Transfer **195**, 176–188 (2017).

27. O. V. Butov, K. M. Golant, A. L. Tomashuk, M. J. N. Van Stralen, and A. H. E. Breuls, "Refractive index dispersion of doped silica for fiber optics," Opt. Commun. **213**(4-6), 301–308 (2002).

28. K. Nagano, S. Kawakami, and S. Nishida, "Change of the refractive index in an optical fiber due to external forces," Appl. Opt. **17**(13), 2080 (1978).